REPORT DOCUMENTATION PAGE

Form Approved
OMB No. 0704-0188

1. REPORT DATE *(DD-MM-YYYY)*
01/24/2012

2. REPORT TYPE
Final Report

3. DATES COVERED *(From - To)*
Jan 2008-Jun 2011; Jan2012

4. TITLE AND SUBTITLE
Effect of Impurities on O and Al Boundary Diffusion in Alumina: Application Alumina Scale Growth in Alloys

5a. CONTRACT NUMBER
N00014-05-1-0232

5b. GRANT NUMBER
12.300

5c. PROGRAM ELEMENT NUMBER

6. AUTHOR(S)
Martin P Harmer - PI
Helen M Chan - CoPI
Jeffrey M Rickman - CoPI

5d. PROJECT NUMBER
11PR03456-01

5e. TASK NUMBER

5f. WORK UNIT NUMBER

7. PERFORMING ORGANIZATION NAME(S) AND ADDRESS(ES)
Lehigh University
Office of Research and Sponsored Programs
526 Brodhead Avenue
Bethlehem, PA 18015-3008

8. PERFORMING ORGANIZATION REPORT NUMBER
11PR03456-01

9. SPONSORING/MONITORING AGENCY NAME(S) AND ADDRESS(ES)
Office of Naval Research
875 North Randolph Street
Arlington, VA 22203-1995

10. SPONSOR/MONITOR'S ACRONYM(S)
ONR

11. SPONSOR/MONITOR'S REPORT NUMBER(S)

12. DISTRIBUTION/AVAILABILITY STATEMENT
"Approved for Public Release; Distribution is Unlimited."

20120312488

13. SUPPLEMENTARY NOTES

14. ABSTRACT
Reactive element (RE) additions are of considerable interest for thermal barrier coating materials. The kinetics of alumina scale growth are controlled by oxygen inward diffusion and/or aluminum outward diffusion along the grain boundaries (gbs). The focus of the program was to determine how RE additions (Y, Hf) affect anion and cation diffusion in alumina. At 1300° C, 500 ppm yttrium slows oxygen gb diffusion by a factor of ~ 5, and increases the corresponding activation enthalpy from 407±20 to 486±34 kJ/mol. Studies on alumina specimens incorporating Ni marker particles suggested that Y also slows Ni outward diffusion. It was also determined that Y-doping retards Cr diffusion in the gb regime by over an order of magnitude.

15. SUBJECT TERMS

16. SECURITY CLASSIFICATION OF:			**17. LIMITATION OF ABSTRACT**	**18. NUMBER OF PAGES**	**19a. NAME OF RESPONSIBLE PERSON**
a. REPORT	**b. ABSTRACT**	**c. THIS PAGE**			Martin P. Harmer
					19b. TELEPHONE NUMBER *(Include area code)* 610-758-4227

Standard Form 298 (Rev. 8/98)
Prescribed by ANSI Std. Z39.18

ONR Final Report - 2012

Abstract

Materials with reactive element (RE) additions are of considerable interest for thermal barrier coating applications because slow-growing alumina scales formed on alloy surfaces can protect the underlying substrate from further oxidation, thereby improving engine lifetime. It is believed that the formation of alumina scales is controlled by oxygen inward diffusion and/or aluminum outward diffusion along the grain boundaries. It remains, however, unclear the extent to which RE additions affect anion and cation diffusion, respectively. Over the course of the program, careful studies of the impact of RE doping on diffusion in alumina were performed.

Novel wedge-geometry, dual-layer alumina samples, both undoped and 500 ppm Y^{3+}-doped, were studied in the temperature regime of 1250 to 1400°C to determine the effect of Y^{3+} on oxygen grain-boundary transport in alumina. The samples consisted of a wedge-shaped, single-phase alumina top layer, diffusion bonded to an alumina/Ni substrate containing a fine, uniform dispersion of Ni marker particles (0.5 vol%). The extent of the alumina spinel oxidation layer was measured as a function of the wedge thickness for a series of heat-treatment conditions. Models of the transport behavior were used to derive values for the rate constants (k) in both the alumina top layer and the alumina/Ni substrate. It was found that the presence of yttrium slows oxygen grain-boundary diffusion in alumina by a factor of approximately 5 (at 1300°C), and increases the corresponding activation enthalpy for oxidation from 407±20 kJ/mol to 486±34 kJ/mol. Microstructural observations suggested that yttrium also slows Ni outward diffusion. A comparison of the different k values revealed that, at 1300°C, the presence of Ni alone enhances transport by approximately a factor of 2 relative to undoped alumina.

The diffusive transport of chromium in both pure and Y-doped fine-grained alumina has been investigated over the temperature range 1250^0–1650^0C. From a quantitative assessment of the chromium diffusion profile in alumina, as obtained from electron microprobe analysis, it was found that yttrium doping retards cation diffusion in the grain-boundary regime by over an order of magnitude.

Technical Section

Technical Objectives

The growth of protective alumina scales on Al_2O_3-forming alloys can be affected by the addition of reactive elements. While a number of theories concerning the "reactive element effect" have been proposed, a full explanation of this phenomenon is not yet available. The overall objective for this program was to conduct a systematic series of model experiments and theoretical analyses in order to determine the separate effects of reactive elements on Al and O grain boundary transport in alumina. The aim will be to better understand, tailor and control alumina scale growth in alloys by undertaking the following assignments:

1. To test whether there is any appreciable effect of reactive elements (Y, Hf, Ba) on the *oxygen diffusivity* by carrying out oxidation anneals on variously doped alumina samples. The samples will contain dispersions of metallic Ni particles, which act as markers to track the rate of oxygen inward diffusion.
2. To develop analytical models and simulation procedures in order to model and simulate the effect of reactive elements on grain-boundary diffusion in alumina.
3. To test the effect of reactive elements on the *aluminum diffusivity* by carrying out diffusion studies of Cr in undoped and doped alumina.

1. Experimental Program

A comprehensive program of research was undertaken to study the fundamental mechanisms of atomic transport in polycrystalline alumina, both undoped and doped with various reactive elements (Y, Hf, Ba), in order to understand the mechanism of alumina scale formation and growth in high temperature superalloys. To measure the rate of inward oxygen diffusion, monolithic samples were processed containing a uniform dispersion of nickel metal particles to act as markers for internal oxidation. [1] Considering the presence of Ni in many high temperature alloys and bond coat compositions, and its importance as a marker particle in our oxidation experiments, the effect of Ni on the oxygen grain boundary diffusion rate was quantified by using a wedge geometry and complementary mathematical analysis. [2] Also, a complementary study of the effect of Y-doping on cation diffusion was conducted using Cr^{3+} as the diffusing species. [5]

2. Experimental Procedure

A.1 Oxygen Diffusion Studies – Monolithic System

a) Sample Preparation

Samples were prepared containing a dispersion of Ni particles to act as markers for internal oxidation. Reduction of NiO was used to form dispersed Ni particles in an alumina matrix. This method produces small (d < 1μm) uniformly dispersed Ni particles in an alumina matrix, and also avoids the hazards of handling sub-micron Ni powders.

Nickel oxide powder was ball milled first in ethyl alcohol for 24 hours to reduce the particle size to less than 1 μm. Then alumina powder was ball milled together with the nickel oxide powder in ethyl alcohol for 24 hours. In order to achieve a volume fraction of 0.5% Ni, 1.5 wt% of NiO was used. In both cases, alumina (99.8%) was used as the milling media, with a ball diameter of ~ 3mm. The slurry was dried and then crushed and milled with an alumina mortar and pestle. The powder mixtures were placed in a graphite die and heat-treated at 650°C for 10 hrs in a 4% H_2-Ar atmosphere. They were subsequently hot pressed at 40 MPa for 3 hrs at 1300°C, at an ambient pressure < 60 mTorr.

Y-doped (500 ppm), Hf-doped (500,100 ppm) and Ba-doped (500 ppm) Al_2O_3 samples (with NiO) were prepared under the same heat treatment conditions as described above, except that the mixed powder was hot-pressed at 1400°C for 3hrs (45 MPa).

b) Oxidation of Samples

The sintered specimens were cut into small rectangular pieces (~ 3x4x2 mm^3). Next the samples were ground with 600-grade SiC paper, and polished down to a 1μm diamond finish using an automated polishing machine. Cleaning was carried out in an ultrasonic bath using the following sequence of solvents (for 30 min each): acetone, ethyl alcohol, and deionized (DI) water. The specimens were subsequently dried in an oven at 90°C for 1 h, and annealed in flowing oxygen in the temperature regime of 1100°C to 1500°C for a range of heat-treatment times.

c) Determination of Thickness of Oxidized Layer

In the surface region, oxidation of the metallic Ni particles to form first NiO and then nickel aluminate spinel ($NiAl_2O_4$) takes place; this region is defined as the oxidized zone. The distance from the polished surface to the boundary of the oxidized layer was measured. The average value (measured from ten different areas) was taken as a measure of the maximum diffusion depth. Figure 1a shows a SEM micrograph of the as-hotpressed sample. Note that for imaging with backscattered electrons, the Ni particles exhibit a brighter contrast than the alumina matrix. Figure 1b shows an SEM micrograph of the cross section of the sample after oxidation for 4h at 1350 °C. The dark matrix phase is alumina, the gray phase is spinel, and the brightest phase is metallic nickel. The region where the Ni particles have been replaced by spinel is marked as the oxidation zone.

In all the samples studied, the extent of the oxidized zone as revealed by SEM was visually well defined. However, in order to identify the position of the reaction front as precisely and reproducibly as possible, the following procedure was adopted. A line was drawn parallel to the surface at a distance $y = y_d$, such that by moving a distance Δy away from the surface, the ratio of the number of Ni particles to that of spinel in the slab thickness Δy, was larger than 50%. Similarly, by moving Δy towards the surface, the corresponding ratio was less than 50%. The value of Δy was set (somewhat arbitrarily) as ~ 5μm, a distance which corresponds approximately to two grain diameters. For each heat-treatment condition, y_d was measured from ten different areas. The average value was taken as a measure of the thickness of the oxidized layer, and hence the oxygen penetration depth.

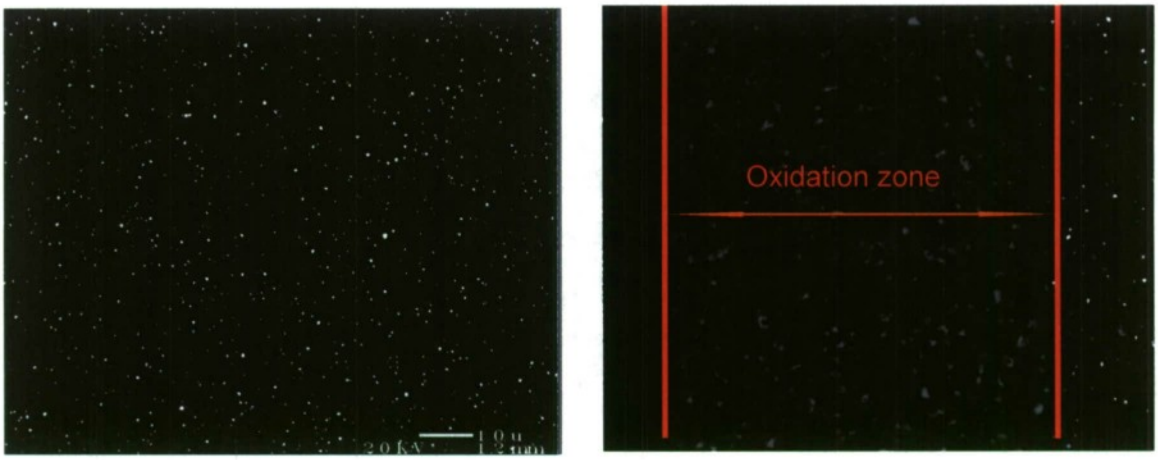

a) b)

Figure 1: SEM micrographs showing the cross section of the undoped alumina sample in the: a) as hot-pressed condition, and b) after oxidation for 4h at 1350 °C, (back-scattered electron contrast).

d) Grain Size Measurement

In order to determine the extent of grain growth during the oxidation anneals, the grain size was determined both in the as-hot-pressed condition, and after heat-treatment. The surface of the samples were polished down to a 1 µm finish and then thermal etched in an argon atmosphere in the temperature regime of 1100°C to 1500°C for a range of heat-treatment times. The etched surfaces were examined by SEM and the grain size was measured using the lineal intercept method.

A.2 Monolithic Samples: Results and Discussion

a) O Diffusion in Undoped and (Y, Hf, Ba)-doped Al_2O_3

The extent of oxidation, as represented by y_d, was measured as a function of heat-treatment time, for isothermal oxygen anneals at various temperature. In every case, parabolic kinetics were observed, i.e., the square of the thickness of the oxidized zone showed a linear dependence with time (see Eqn below),

$$y_d^{\,2} = k\,t$$

where y_d is the thickness of the oxidized layer, t is time, and k is the parabolic rate constant. In general, for the same heat-treatment temperature and time, it was found that the thickness of the oxidation layer was lower in the case of the Y-doped samples, compared to the undoped (see for example, Figure 2). At each temperature, the value of the parabolic rate constant (k_c) was determined by linear fits to the data plotted in Figure 3. The results for undoped and Y doped are summarized in Table I. A graph depicting the behavior of the Hf doped sample is shown in Figure 4. Preliminary data for Ba-doped alumina is shown in Figure 5.

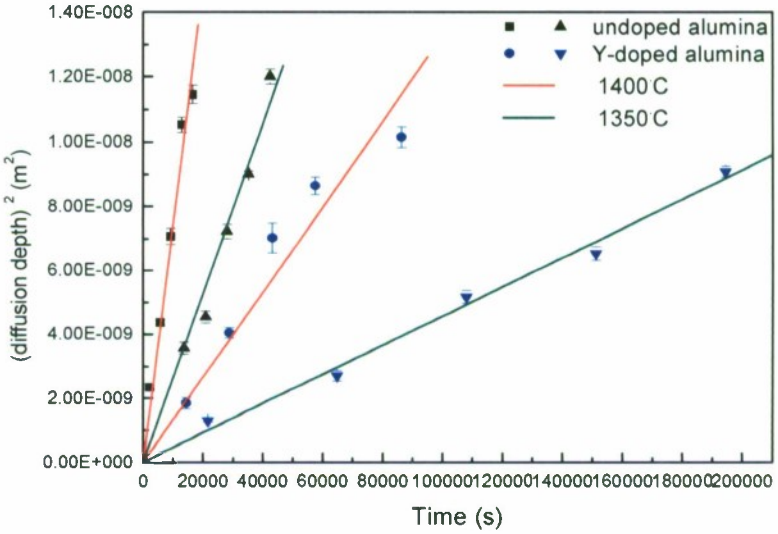

Figure 2: Graphs of the square of the thickness of the oxidized layer, plotted as a function of annealing time at 1350 and 1400 °C. Comparison between undoped alumina and 500ppm Y-doped alumina.

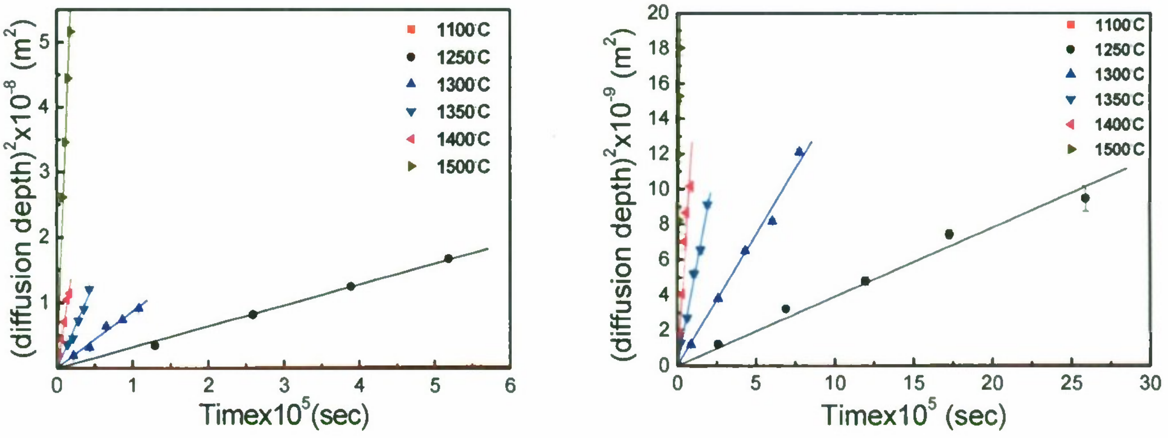

a)

b)

Figure 3: Graphs of the square of the thickness of the oxidized layer, plotted as a function of annealing time, for different heat-treatment temperatures: a) undoped alumina, b) 500ppm Y-doped alumina.

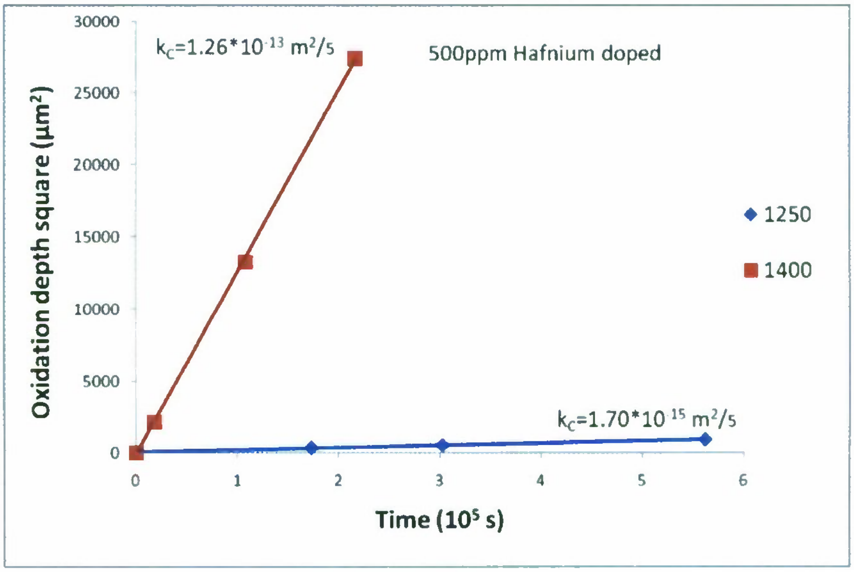

Figure 4: Hf-doped alumina: Graphs of the square of the thickness of the oxidized layer, plotted as a function of annealing time at 1250 and 1400 °C.

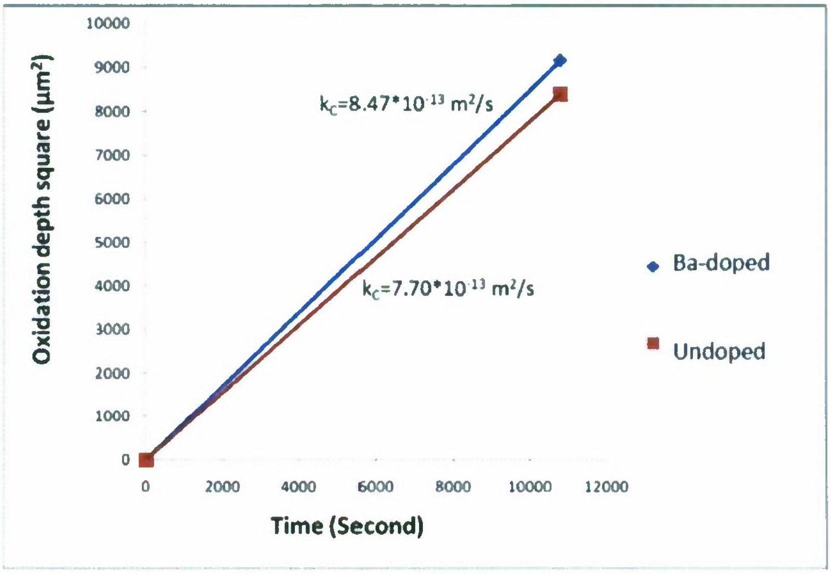

Figure 5: Graphs of the square of the thickness of the oxidized layer, plotted as a function of annealing time at 1400 °C: Comparison between 500 ppm Ba-doped and undoped alumina.

By comparing the values of the ratio of the rate constants for undoped alumina, versus Y-doped, it can be seen that the beneficial influence of the Y is greatest at the lowest annealing temperature (1100 °C), where the rate constant is a factor of 14 times less. With increasing temperature, however, the effect of the Y is diminished. Also, Table II summarizes the results including previous ones and Hf-doped alumina. For the purposes of comparison, it is necessary to normalize the *k* values with respect to grain size. Table III shows values of the ratio for the various dopants, assuming a uniform grain size. It can be seen from Table III that both Y- and Hf-doping have a beneficial effect in terms of retarding the oxygen transport kinetics in alumina. At 1250 °C, the extent of this effect is of the order of a factor of 7-8, and is similar for the two dopants. In contrast, the addition of Ba increases the rate of oxygen grain boundary diffusion. Note that although the graphs depicted in Figure 5 were very similar, after correction for the influence of grain size, it was found that 500ppm Ba increases *k* by about a factor of 2. More studies are underway to confirm this trend, and to understand the differences in behavior between the different dopant species.

Table I. Values of the parabolic rate constants determined for undoped and Y-doped alumina

k_c (m^2/s)	1100°C	1250°C	1300°C	1350°C	1400°C	1500°C
Undoped	7.62×10^{-16}	3.2×10^{-14}	8.67×10^{-14}	2.64×10^{-13}	7.47×10^{-13}	3.05×10^{-12}
500-ppm Y doped	5.29×10^{-17} *	3.91×10^{-15}	1.48×10^{-14}	4.57×10^{-14}	1.33×10^{-13}	1.05×10^{-12}
$k_c/k_c(Y)$	14	8	6	6	6	3

**data from two experiments only*

Table II. Values of the parabolic rate constants (k) determined for undoped and doped alumina

MATERIAL	**k (m^2/s) 1250 °C**	**k (m^2/s) 1400 °C**
Undoped	3.09×10^{-14}	7.77×10^{-13}
Y - doped	4.31×10^{-15}	1.34×10^{-13}
Hf - doped	1.70×10^{-15}	1.26×10^{-13}
Ba - doped	_	8.47×10^{-13}

Table III. Ratio of the parabolic rate constants value (k) for undoped versus doped alumina (values normalized to account for differences in grain size)

	k (undoped)/ k (doped)	
MATERIAL	**1250 °C**	**1400 °C**
Y - doped	7.0	6.0
Hf - doped	7.9	3.2
Ba - doped	_	0.53

The Arrhenius plot for k_c is shown in Figure 6 for both the undoped and Y-doped alumina. The values of the activation energies for oxygen diffusion were determined to be 425.2 ± 8 kJ/mol, and 498.5 ± 2 kJ/mol respectively.

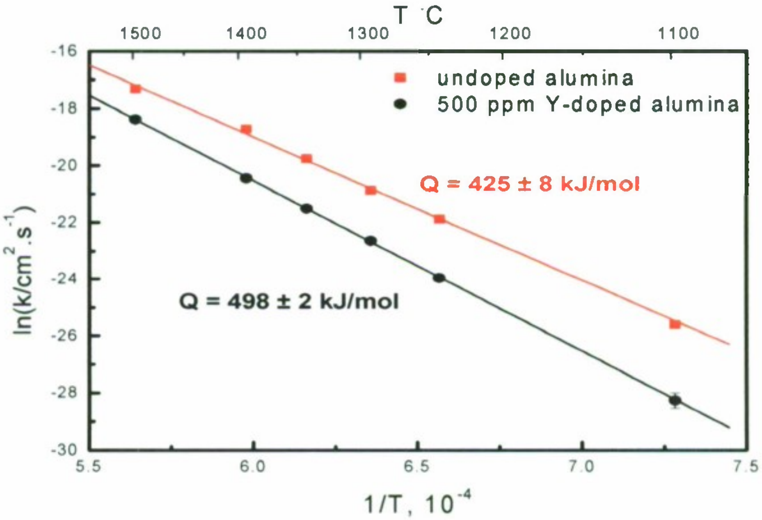

Figure 6: Arrhenius graphs of the rate constants (k_c) for undoped and 500 ppm Y-doped alumina.

b) Oxidized Surface Comparison

Depending on the heat treatment time and temperature, some of the samples also exhibited the formation of spinel at the free surface, formed presumably by the oxidation of Ni, which had diffused to the surface. To test whether the presence of the porous, surface spinel layer was providing an additional barrier to inward oxygen diffusion, oxidation experiments were performed for samples where the spinel layer was periodically removed by grinding. Since the depth of oxidation in these samples was practically identical to those where the surface layer was left intact, it was concluded that the surface oxidation was not playing a significant role in our findings.

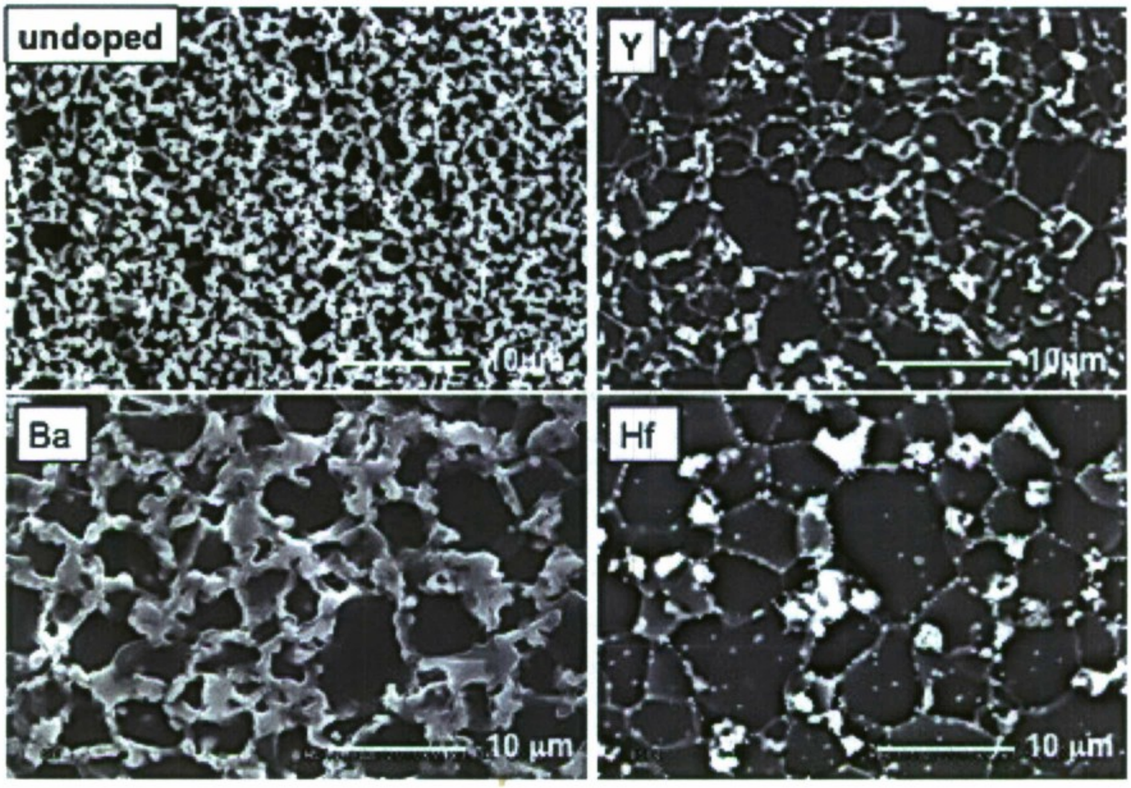

Figure 7: SEM micrographs depicting the free surfaces of the samples after annealing in oxygen for 4 h at 1400°C for undoped alumina, Y-doped alumina, Ba-doped alumina and Hf-doped alumina.

c) Grain Size Measurement and Grain Boundary Chemistry

The average grain sizes of the undoped samples both in the as-hot-pressed condition, and after the oxidation anneals, are shown in Table IV. It can be seen that for all the samples, the extent of grain growth during the oxidation heat-treatments was minimal. It is also worth noting that because the grain sizes of the undoped and Y-doped specimens were identical (within experimental scatter) this was not a factor in causing the difference in oxygen transport kinetics.

Preliminary studies on compositional segregation at the alumina grain boundaries have revealed an enhancement in the Ni content (see Figure 8). Work is on going to establish whether the Ni grain boundary concentration is uniform throughout the sample, and if the presence of Y affects the Ni concentration.

Table IV. Grain size of undoped and Y-doped alumina samples for different heat-treatments

	As-hot-pressed	1250°C		1300°C		1350°C		1400°C		1500°C	
		t (hr)	G.S. (µm)	t (hr)	G.S. (µm)	T (hr)	G.S. (µm)	t (hr)	G.S. (µm)	t (hr)	G.S. (µm)
undoped	1.83±0.27	144	1.91±0.24	30	1.97±0.3	12	1.89±0.3	5	2.05±0.31	5	2.95±0.34 *
500 ppm Y doped	2.13±0.25	720	2.15±0.37	216	2.1±0.33	54	2.09±0.31	24	2.29±0.45	5	2.73±0.53

* The specimen was from the 2nd batch heat treated sample with initial grain size 1.46±0.15µm.

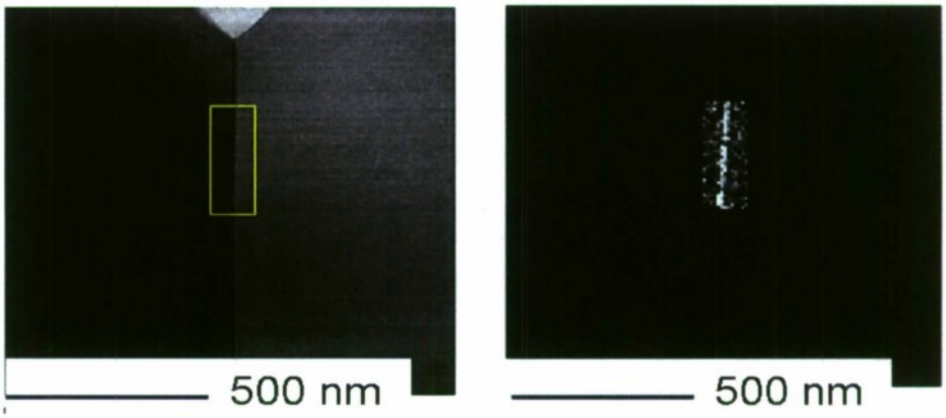

a) *b)*

Figure 8. STEM images of a grain boundary within the oxidized zone of an undoped alumina annealed at 1400°C for 3 h, showing the segregation of Ni along the boundary. a). Annular dark field image, b) Ni map.

B.1 Oxygen Diffusion Studies – Wedge system

a) Sample Preparation

500 ppm Y^{3+}-doped alumina powder (>99.99%) was hot-pressed at 1300°C for 12 h at 45 MPa at an atmospheric pressure of less than 60mTorr, and then cut into ~3mm-thick slices. One

side of a slice was polished down to 1 μm and the other side was ground until both sides were parallel. The as-hot-pressed 500 ppm Y^{3+}-doped alumina/Ni composite was made by following the procedure described in an earlier paper[1]. After hot-pressing, it was also cut into ~3mm-thick slices, polished and ground as outlined above.

Several narrow strips of a thin Ir coating (width ~ 0.5mm) were sputtered onto the polished surface of the alumina/Ni composite prior to joining to mark the original position of the bi-layer interface. The Y^{3+}-doped alumina and alumina/Ni samples were then assembled with the polished sides facing each other, and subsequently hot-pressed at 1300°C for 15 h at 45 MPa at an atmospheric pressure less than 60mTorr. The as-hot-pressed bi-layer sample was then cut into small rectangular pieces (~8×3×3mm^3). Each piece was glued (alumina layer facing outwards) onto a 3°-inclined surface of a stub (Fig. 9-a). First, the alumina layer was ground using a 10-μm fixed diamond disk until a small area of the alumina layer on one side was removed; the surface was then polished to a 1 μm finish (Fig. 9-b). This procedure was adopted to ensure that the depth of the alumina layer started from zero and increased gradually. It also minimized the possible influence of oxygen diffusion from the side of the sample.

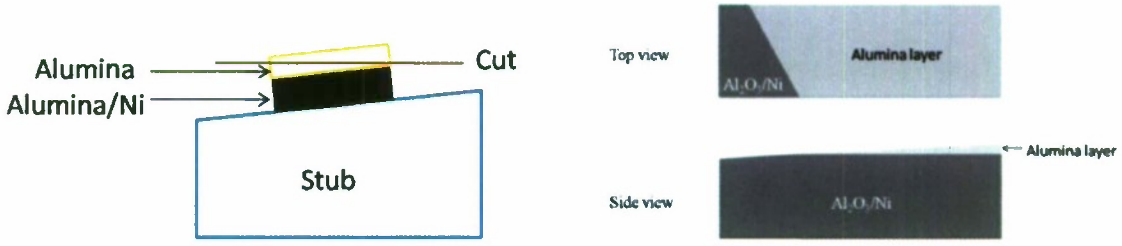

a

b

Figure 9: Schematic showing a) the procedure for cutting the bi-layer specimen to obtain the wedge geometry; and b) the top and side view of wedge-shaped bi-layer specimen used for oxidation experiments.

b) Oxidation of Samples

The top alumina layers of the Y^{3+}-doped wedge samples were polished down to a 1 μm diamond finish using an automated polishing machine. The samples were cleaned in an ultrasonic bath using first acetone, then ethyl alcohol followed by deionized water, for 30 minutes each. After cleaning, a wedge specimen was placed in an alumina crucible (99.8%) with high-purity alumina powder around it. Oxidation of the samples was carried out in an oxygen-flow tube furnace in the temperature range of 1300 to 1400°C for a specified period of time. Finally, the samples were sectioned and polished again down to 1 μm, and the depth of the alumina layer (x) and the size of the corresponding oxidized zone (y) were measured from backscattered electron images (BSE) obtained in a scanning electron microscope (SEM) operated at 20KV.

c) Determination of Diffusion Depth

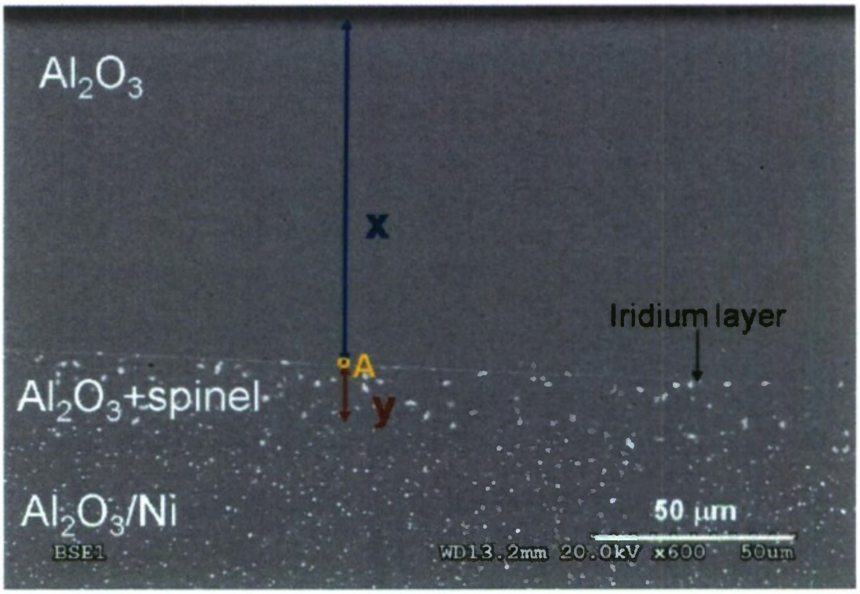

Figure 10: Scanning electron micrograph showing the cross section of the undoped wedge sample after oxidation at 1350°C for 20 h. (back-scattered electron contrast).

Figure 10 shows a cross section of an undoped wedge sample that was oxidized for 20 h at 1350°C and examined under SEM using BSE contrast. Y^{3+}-doped wedge samples look similar as this under SEM. The thickness of the alumina wedge layer, x, and that of the corresponding alumina/spinel layer, y, as shown in the figure, were determined.

B.2 *Results*

a) Microstructure

The average grain sizes of the Y^{3+}-doped wedge samples, both in the as-hot-pressed condition and after the heat treatment, were determined using the linear intercept method, incorporating a stereological factor of 1.5. The values are listed for both the wedge layer and the alumina/Ni substrates in Table V. In order to evaluate the maximum extent of grain growth during the oxidation anneal, grain sizes were determined for the longest heat-treatment time at each temperature. It can be seen that for the Y^{3+}-doped sample, the size of the alumina grains in both layers was within experimental scatter.

Table V: Grain sizes of Y^{3+}-doped alumina wedge samples for different heat-treatment conditions

	As-hot-pressed	1300°C (490 h)	1350°C (120 h)	1400°C (80 h)
Alumina layer	2.58±0.25	2.77±0.35	2.83±0.41	3.12±0.43
Alumina/Ni substrate	2.96±0.37	3.02±0.35	3.21±0.45	3.42±0.43

b) Simplified Transport Models

Fig.11 shows a set of experimental data for an undoped wedge sample oxidized at 1350°C for 60 h in which y^2 is plotted versus xy. It is noted that the resulting curve has a linear regime for only a limited range of x (and therefore a limited range of y). The linear regime corresponds to the pseudo-steady state diffusion process while the rest corresponds to transient state. Therefore, two simplified models were used to describe two regions respectively.

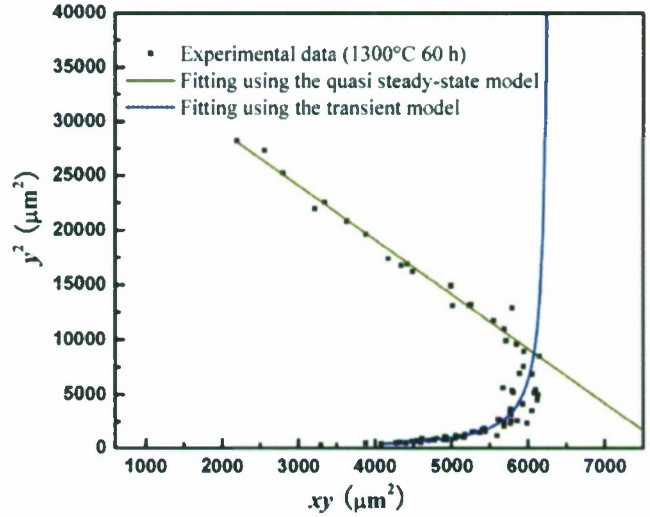

Figure 11: Graph depicting both the experimental results (1350°C for 60 h) and the fit to the data using the quasi steady-state model (Eq. 1) and the transient model (Eq. 2).

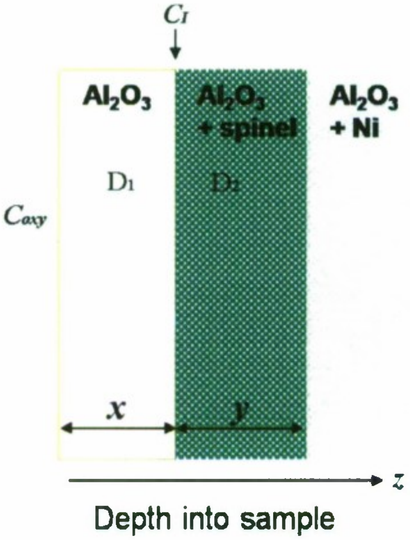

Figure 12: Schematic of the bi-layer alumina samples used for developing transport models.

Consider the schematic of the bi-layer system shown in Fig. 12. For the pseudo-steady state model (C(z=x+y)=0), given the diffusivities D_1 and D_2 in these layers, respectively, and the oxygen concentration, $C(z)$, at the surface, $C(z=0)=C_S$, and at the layer interface, $C(z=x)=C_1$, respectively, the relationship between oxygen transport rate constants in the alumina layer and in the alumina/Ni layer obtained using Fick's Law is

$$\frac{y^2}{t} = k_2 - 2\left(\frac{k_2}{k_1}\right)\frac{xy}{t} \qquad . \qquad (1)$$

where y is the depth of the oxidized (i.e., Al_2O_3/spinel) layer, C_{Ni}^0 is the initial Ni concentration, and the rate constants k_1 and k_2 are given by $k_1 = (2C_s / C_{Ni}^0)D_1$ and $k_2 = (2C_s / C_{Ni}^0)D_2$. A linear regression for first portion of the curve yields the fitting line (and hence D_2/D_1) shown in Fig. 11.

For $x > x'$, where x' locates the nose of the curve, the pseudo-steady state has not been reached and transient behavior is observed. In reality, of course, there is a narrow range of x values over which this transition occurs, but for simplicity we will identify one critical value, namely x', where $x' \approx x_c$. The diffusive behavior in the transient regime can be modeled simply by assuming that C_1 is essentially zero for cases in which $x > x'$. In the late-stage transient regime where $t > x^2 / 6D_1$ one obtains the approximate relation

$$\frac{y}{t} \approx \frac{C_s D_1}{C_{Ni}^0}\frac{1}{x} - \frac{C_s}{6C_{Ni}^0}\frac{x}{t} \qquad . \qquad (2)$$

The best fit for data points for which $x > x'$, based on Eq. (2), is also displayed in Fig. 11. We note that the value of x' was estimated from the location of the nose of the curve and that the fitting parameters were relatively insensitive to the value of x' chosen. It can be seen that, taken together, the two curve fits describe the data over a wide range of layer thicknesses.

c) Kinetic Parameters

Fig. 13 presents the graphs of y^2/t versus xy/t of the undoped and Y^{3+}-doped wedge samples, respectively, for a series of heat treatments at different temperatures. By applying the foregoing analysis to these data sets, values of k_1, k_2, D_1 and C_s / C_{Ni}^0 were obtained as a function of temperature. (In this notation, the subscript 1 denotes the outer wedge layer, whereas the subscript 2 denotes the alumina/Ni substrate.) These findings are summarized in Table VI for both the undoped and Y^{3+}-doped samples over the range of temperatures studied. The stated uncertainties in the values of *k* represent the spread in the *k* values obtained at the same temperature, but for different heat-treatment times.

The ratio of $k_1/k_1(Y)$ reflects the influence of yttrium on oxygen transport in alumina in the absence of nickel particles. Over the range of temperatures studied, the rate constant is greater by up to a factor of 3 at 1300°C in the undoped alumina layer. However, the average grain size, *d*, in the undoped alumina layer was consistently larger than that of the Y^{3+}-doped layer (i.e., $d_1/d_1(Y) \sim 1.6$, where *d* is the grain size). Assuming grain-boundary transport is dominant, the apparent diffusivity will scale with the inverse of the grain size and, if a grain-size correction is applied, it can be seen that the presence of yttrium reduces oxygen grain-boundary diffusion in alumina by up to a factor of 5 (that is, 3×1.6) at 1300°C.

What about the effect of Ni on oxygen transport? At 1300°C, k_2/k_1 (the rate constant ratio of the alumina/Ni substrate relative to the upper alumina wedge layer), is approximately 3. However, the grain size in the alumina wedge layer was larger than that of the substrate ($d_1/d_2 \sim 1.4$). If the ratio k_2/k_1 is corrected to account for the grain size difference, then the finding is that nickel increases oxygen grain-boundary transport in alumina by a factor of about 2 (i.e. 3/1.4) in the temperature range studied. Interestingly, the value of the corresponding ratio in the Y^{3+}-doped wedge sample ($k_2(Y)/k_1(Y)$) was close to unity at all the temperatures studied. In this case, the average grain sizes of the two layers were within experimental scatter. The implication, therefore, is that in the presence of Y, the effect of Ni on enhancing oxygen transport is negated.

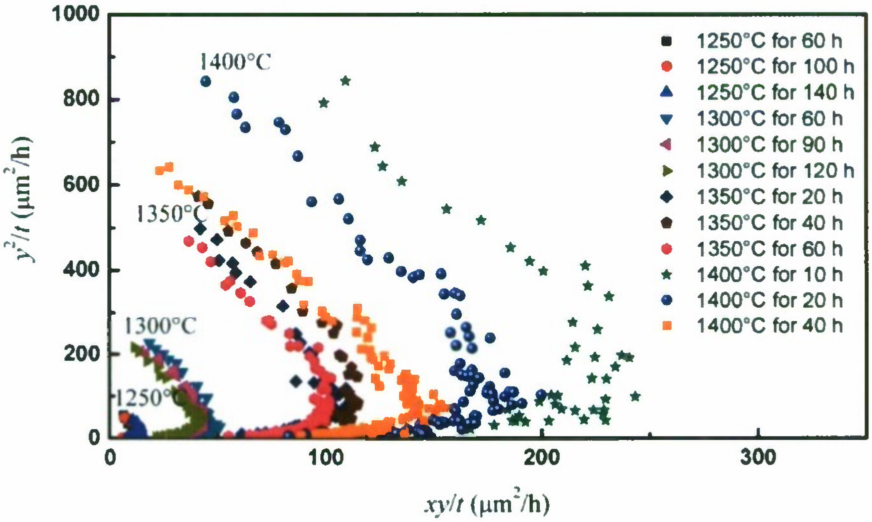

a) undoped wedge samples

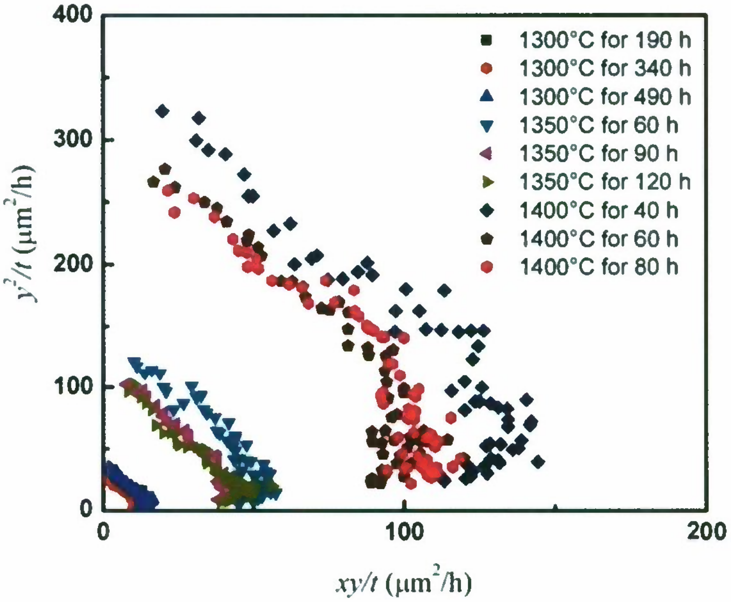

b) Y-doped wedge samples

Figure 13: Graphs showing the relationship at different temperatures between the square of the oxidized layer thickness (y^2), and the product of y with the depth of the alumina wedge layer (x); the quantities on both axes were normalized with respect to the annealing time (t).

To analyze the oxidation kinetics, the logarithm of the rate constants was plotted versus the reciprocal of the absolute temperature in Fig. 14, and the expected Arrhenius behavior was obtained. The activation energies for oxygen diffusion, *E*, were determined from a least-squares fit to these plots, and the values corresponding to the different material layers are tabulated in Table VII. In the case of the undoped and 500 ppm Y^{3+}-doped alumina outer wedge layers, the activation energies were found to be E_1(u)=407±20 kJ/mol and E_1(Y)=486±34 kJ/mol, respectively. For the undoped and 500 ppm Y^{3+}-doped alumina/Ni substrate layers, the corresponding values were determined to be E_2(u)=381±30 kJ/mol and E_2(Y)=489±37 kJ/mol, respectively. It can be seen that the values for the undoped layers (E_1(u), E_2(u)) agree within experimental scatter, and similarly for the Y-doped layers (E_1(Y), E_2(Y)). This agreement implies, in turn, that the presence of Ni does not significantly influence the activation energy, a result that was confirmed at the 5% level of significance by applying a standard statistical test of the equality of means.

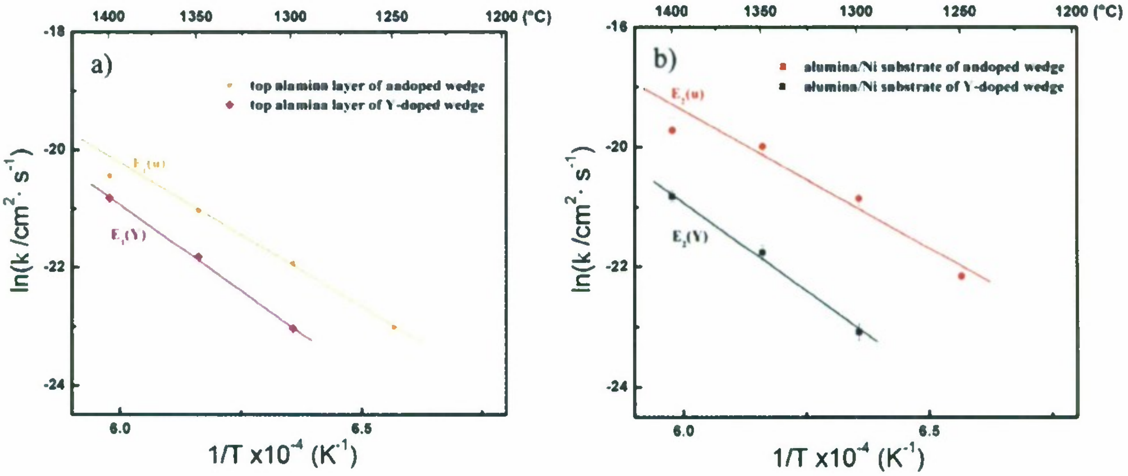

Figure 14: Arrhenius plots of the rate constants for a) the alumina layer and b) the alumina/Ni substrate of wedge samples, both undoped and 500 ppm Y^{3+}-doped. (The solid lines are least-squares fits to the data.)

Table VI: A summary of the kinetics data for the undoped and Y^{3+}-doped wedge samples

Temp	undoped		Y-doped		ratio			undoped	
(°C)	k_1 (m^2/s)	k_2 (m^2/s)	$k_1(Y)$ (m^2/s)	$k_2(Y)$ (m^2/s)	k_2/k_1	$k_2(Y)/k_1(Y)$	$k_1/k_1(Y)$	D_1(m_2/s)	C_s/C_{Ni}
1250	$(1.01\pm0.06)\times10^{-14}$	$(2.39\pm0.29)\times10^{-14}$			2.37±0.45			$(8.46\pm0.53)\times10^{-15}$	0.49±0.03
1300	$(3.00\pm0.17)\times10^{-14}$	$(8.74\pm0.99)\times10^{-14}$	$(9.91\pm1.06)\times10^{-15}$	$(9.35\pm1.24)\times10^{-15}$	2.91±0.53	0.94±0.26	3.03±0.55	$(3.41\pm1.39)\times10^{-14}$	0.40±0.12
1350	$(7.35\pm0.61)\times10^{-14}$	$(2.08\pm0.26)\times10^{-13}$	$(3.32\pm0.55)\times10^{-14}$	$(3.52\pm0.43)\times10^{-14}$	2.83±0.64	1.06±0.37	2.21±0.66	$(8.31\pm2.34)\times10^{-14}$	0.41±0.16
1400	$(1.33\pm0.43)\times10^{-13}$	$(2.72\pm0.52)\times10^{-13}$	$(9.14\pm0.94)\times10^{-14}$	$(9.02\pm0.82)\times10^{-14}$	2.05±1.55	0.99±0.21	1.46±0.69	$(2.77\pm0.73)\times10^{-13}$	0.19±0.01

Table VII: Activation energies for oxygen diffusion in alumina

	wedge experiment				Monolithic experiment	
	undoped		Y-doped		undoped	Y-doped
	Alumina	Alumina/Ni	Alumina	Alumina/Ni		
E (kJ/mol)	407±20	381±30	486±34	489±37	430±40	497±8

d) Exact Transport Model

The oxidation kinetics in the bi-layer alumina sample can be described by a reaction-diffusion model that reflects oxygen transport and the chemical reaction between nickel and oxygen to form spinel. The bi-layer geometry is shown in the schematic in Fig. 12, where the depth of the alumina layer, x, is fixed. For this geometry, the oxygen concentration, C, and nickel concentration, C_{Ni}, are obtained from the equations

$$\begin{cases} \dfrac{\partial C}{\partial t} = D_1 \dfrac{\partial^2 C}{\partial z^2} & \text{for} \quad 0 < z \le x \\ \dfrac{\partial C}{\partial t} = D_2 \dfrac{\partial^2 C}{\partial z^2} - r(C, C_{Ni}, T) & \text{for} \quad z > x \\ \dfrac{\partial C_{Ni}}{\partial t} = -r(C, C_{Ni}, T) & \text{for} \quad z > x \end{cases} , \qquad (3)$$

subject to the initial and boundary conditions

$$\begin{cases} C_{Ni}(t=0, z \ge x) = C_{Ni}^0; \quad C_{Ni}(t=0, \; 0 < z < x) = 0; \\ C(t=0, z>0) = 0; \qquad C(z=0) = C_s; \\ \left.\dfrac{\partial C}{\partial z}\right|_{z\to\infty} = 0; \qquad D_1 \left.\dfrac{\partial C}{\partial z}\right|_{z=x^-} = D_2 \left.\dfrac{\partial C}{\partial z}\right|_{z=x^+}; \end{cases} \qquad (4)$$

where C_s is oxygen surface concentration (i.e. the oxygen solubility in alumina), C_{Ni}^0 is the initial concentration of Ni in alumina/Ni substrate, and D_1 and D_2 are the apparent diffusivities in the alumina top layer and the underlying layer, respectively.

For the purposes of the analysis, it is convenient to recast these equations in dimensionless form. By defining the dimensionless parameters $\tau = tD_1 / x^2$, $z^* = z / x$, $C^* = C / C_s$, $C^*_{Ni} = C_{Ni} / C^0_{Ni}$ and $\Phi^2 \equiv k_r x^2 C^0_{Ni} / D_1$, the reaction-diffusion equations become

$$\begin{cases} \dfrac{\partial C^*}{\partial \tau} = \dfrac{\partial^2 C^*}{\partial z^{*2}} & for \quad 0 < z^* \leq 1 \\ \dfrac{\partial C^*}{\partial \tau} = \dfrac{D_2}{D_1}\dfrac{\partial^2 C^*}{\partial z^{*2}} - \Phi^2 C^* C^*_{Ni} & for \quad z^* > 1 \\ \dfrac{\partial C^*_{Ni}}{\partial \tau} = -\Phi^2 C^* C^*_{Ni} (\dfrac{C_s}{C^0_{Ni}}) & for \quad z^* > 1 \end{cases} \tag{5}$$

Solving these equations numerically using a higher-order finite- difference approximation (i.e., the numerical method of lines), C^* and C^*_{Ni} were calculated for different reduced times, τ , as shown in Fig. 15. The depth of alumina/spinel layer was calculated via $y^* = z^*\big|_{c^* \approx 1\times10^{-3}} - 1$ where, for practical purposes, the oxygen concentration was taken to be zero when $C^* < 1 \times 10^{-3}$.

The results are displayed in Fig. 16, and it can be seen that the numerical data form the characteristic 'C'-shaped curve and that there is good agreement between with the experimental data in the transient regime. The discrepancy between the numerical and the experimental results in the pseudo-steady state regime may be caused by Ni diffusion into the wedge along the grain boundaries. (It should be noted that the reaction-diffusion model does not incorporate Ni diffusion.) The role of Ni diffusion in the wedge geometry and in the corresponding reaction-diffusion models of oxidation is the subject of ongoing investigations.

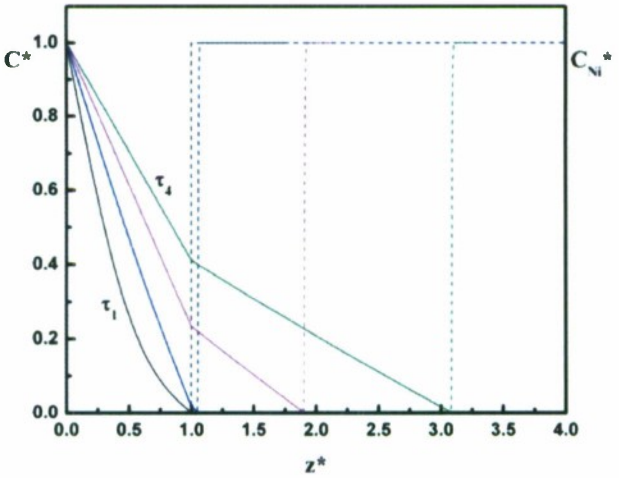

Figure 15: Calculated oxygen and Ni concentration profiles in bilayer alumina samples at different times τ *(*$\tau_1 < \tau_4$*) according to Eq. (5).*

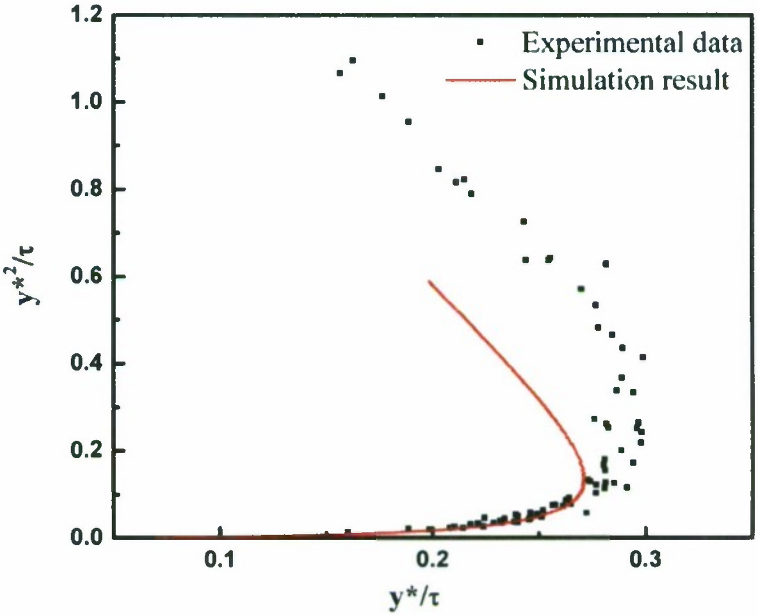

Figure 16: Comparison of experimental data and numerical results plotted in terms of the dimensionless parameter y^{*2}/τ *(related to the square of the depth of alumina/spinel layer,* y^2*), versus the dimensionless parameter* y^*/τ *(related to the product of the depth of alumina layer and the depth of alumina/spinel layer, xy) for the undoped wedge sample oxidized at 1350°C for 60 h.*

C. Grain-Boundary Energy and Misorientation

The goal of much of our work to date has been to elucidate the impact of rare-earth dopants on grain-boundary cationic and anionic transport in alumina. As these dopants are found to segregate preferentially to grain boundaries, it is clearly of interest to ascertain whether grain-boundary segregants alter boundary structure and energetics and, thereby, boundary transport. This may be accomplished by, for example, examining the geometry of grooves where grain boundaries intersect a free surface, and then using an analysis due to Mullins [3] to infer the distribution of relative boundary energies in both undoped and doped samples.

More specifically, to assess the impact of dopants on the distribution of grain-boundary energies, we have employed atomic-force microscopy (AFM) to acquire the shape profiles of thermally etched surfaces in both undoped and doped polycrystalline alumina. From these profiles we have taken cuts normal to different grain boundaries to obtain surface height maps of grain-boundary grooves. Automated analyses of these maps then permitted us to measure the associated dihedral angles (see Fig. 17) and to calculate the corresponding grain-boundary energies. Meaningful cumulative distributions of dihedral angle and energy were tabulated using populations of several hundred grains.

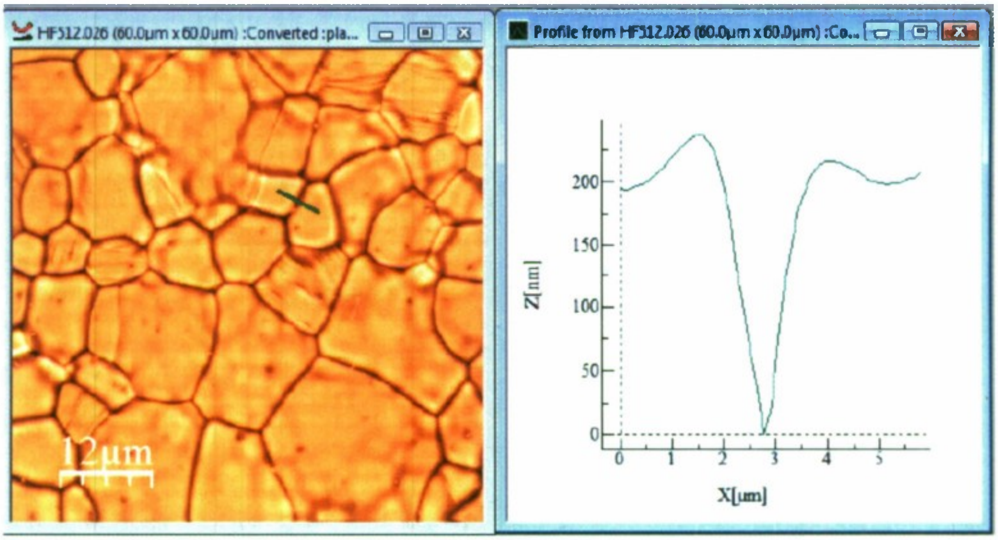

Figure 17: AFM image showing surface topography of undoped alumina sample thermally etched for 3 h at 1500 °C (LHS). Depth profile for selected grain boundary section (RHS).

Given our previous studies of the role of doping in altering the creep response of ceramic oxides, we selected yttrium and hafnium for our investigations here. Figure 18 shows the cumulative distribution of boundary dihedral angles for both undoped and doped alumina based on grain populations of about 200 grains for each system. It can be seen that doping leads to the same qualitative shift in the distribution to smaller dihedral angles. The values of the means for the dihedral angle measurements were determined to be as follows: Hf-doped alumina (138.1 ± 6.3 deg.), Y-doped alumina (135.6 ± 8.3 deg.), undoped (142.6 ± 10.0 deg.). We are now in the process of calculating the corresponding distributions of grain-boundary energies and assessing the significance of doping in determining these distributions.

a)

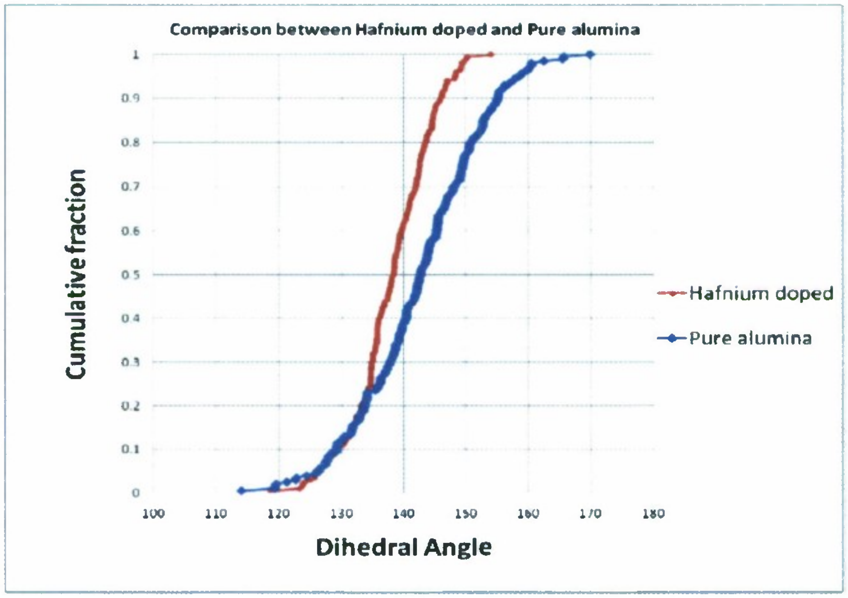

b)

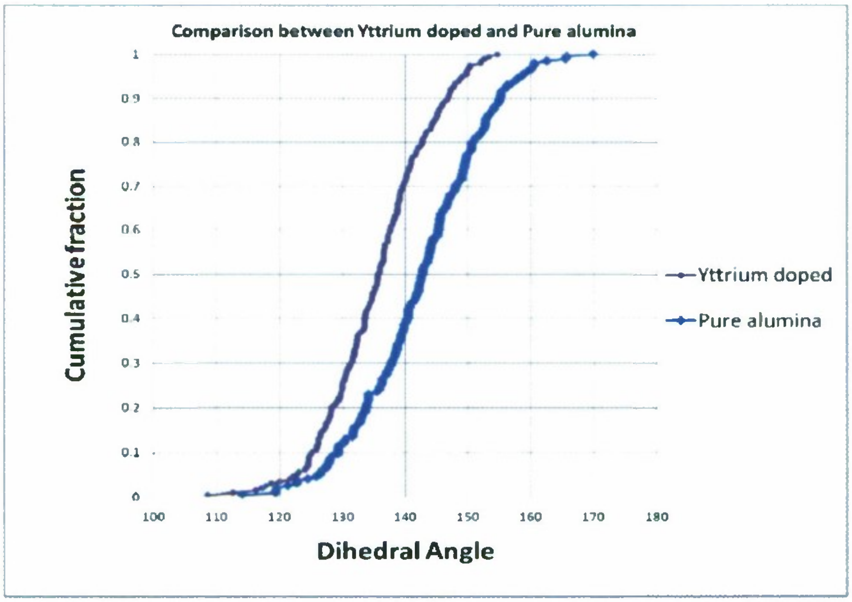

Figure 18: Influence of dopant on cumulative grain boundary dihedral angle distributions in alumina: a) Hf-doping (500 ppm), b) Y-doping (500 ppm)

D. Cr Diffusion Studies

a) Introduction

In order to characterize cation transport in alumina, the diffusion of chromium in both undoped and Y-doped fine-grained alumina has been investigated. In this work, Cr^{3+} was employed as a plausible substitute for Al^{3+} given their similar ionic radii, isovalency, and the mutual solubility of chromia and alumina at temperatures exceeding 900^{0}C. More specifically, Cr^{3+} diffusion profiles were acquired from electron microprobe analyses over a range of temperatures and subsequently used to extract activation energies for grain-boundary diffusion.

b) Sample Preparation

Polycrystalline samples were prepared using ultra high-purity alumina powder (AKP-53, Sumitomo Chemical America, New York, NY). Yttrium doping (at the 100 ppm level) was achieved by adding suitable amounts of yttrium nitrate solution. The powders were placed in graphite dies and heat-treated in vacuum at 1200 °C for 12 hrs under 45 MPa of pressure, resulting in samples of about 99.7% and 97.64% relative density, for the undoped and Y-doped samples, respectively. Grain sizes were determined from SEM micrographs using the linear intercept method, assuming a grain size of 1.5 times the mean intercept. Initial average grain sizes were determined to be about 1.95 μm for the undoped alumina, and about 0.76 μm for the Y-doped samples. The sintered specimens were cut into small cubic pieces with dimensions of about 5x5x5 mm^3. Sapphire samples (obtained from Insaco Inc., Quakertown, PA) with dimensions of about 5x5x1mm^3 were also prepared. The specimens were cleaned by submerging them in a beaker of acetone placed in an ultrasonic bath for 10 minutes. This procedure was repeated, but with ethyl alcohol and then deionized water. The samples were then dried in an oven at 90 °C for 15 minutes.

Next, the sintered alumina samples were covered in excess high-purity Cr_2O_3 powder and compacted in an acid-washed alumina ceramic crucible. Isothermal annealing was carried out in air at temperatures in the range 1250 – 1650 °C for times ranging from 35-336 hrs. (Note that in order to minimize grain growth during the diffusion anneals, samples were pre-heated at the diffusion temperature for 5 days.) The resultant samples were cut in two equal parts and mounted in a conducting epoxy. They were subsequently ground with 600-grade SiC paper and then polished (using diamond polishing media) down to a 1µm finish.

c) Acquisition of Compositional Profiles

The samples were carbon-coated and analyzed for all three elemental components in an electron microprobe (JEOL JXA-733 super probe) using $K_{\square}$ characteristic x-ray lines. The operating conditions were as follows: accelerating voltage 12 kV, sample absorption current of 40 nA, and beam diameter ~ 1µm (adjusted for excitation volume). The 99% confidence interval detection limit was less than 0.1 elemental wt.% for each constituent. The concentration profiles were obtained by scanning perpendicular to an edge of the sample. Depending on the diffusion depth, a linescan consisted of about 10-18 analysis points, with an acquisition time of 120s per point. The areas analyzed were selected so as to avoid pores, and were sufficiently separated so that there was no overlap of the excitation volumes. For a given sample, about 10-15 x-ray intensity linescans were obtained. We then defined the average concentration at a given depth, $C_{\text{avg}}(x)$, as the average over sampling points on different linescans at a depth x, and report our results relative to C_0, the chromium concentration at the surface. During the diffusion anneals, it was found that a dense layer of chromia was formed at the surface of the alumina samples (see

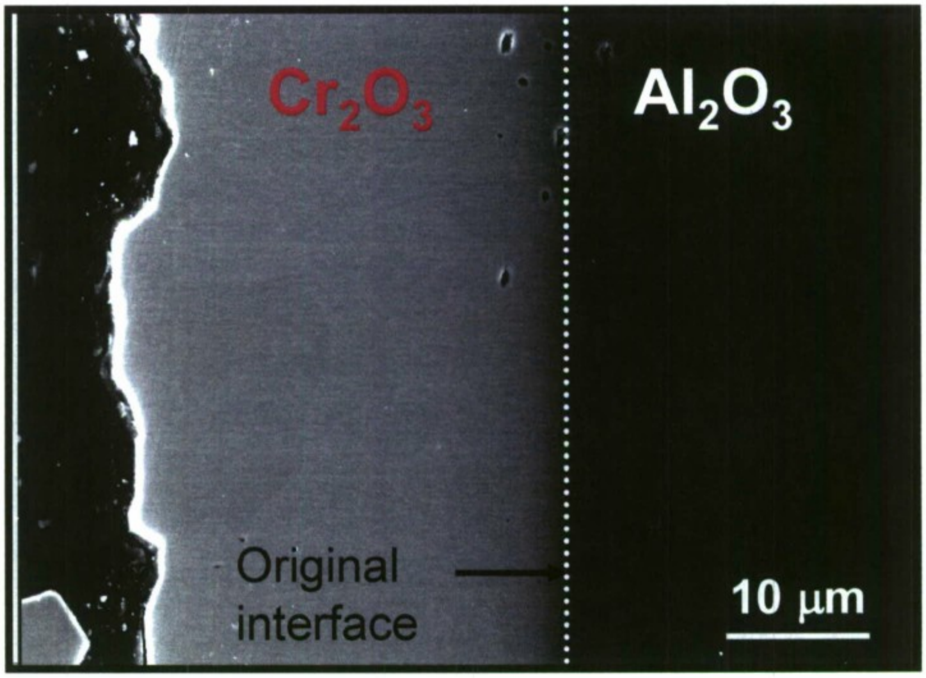

Figure 19: SEM micrograph of sectioned sample, showing dense chromia layer at the surface of the sapphire.

Figure 19). Effectively, therefore, there is a chromia-alumina diffusion couple with interdiffusion of the different cations.

d) Results and Discussion

In the polycrystalline samples it was determined that the experimental conditions were consistent with the so-called Type B kinetic regime in Harrison's classification scheme, wherein the average grain size is sufficiently large that the diffusion fields from grain boundaries are essentially independent. In this limit, the concentration profile can be regarded, to a good approximation, as a superposition of contributions from the distinct boundaries. It is therefore sensible to interpret the results in terms of the Whipple-LeClaire model that assumes a power-law dependence of the log of the concentration far from the source. Weighted linear regression was employed to fit the linear tail of the acquired concentration profiles. The fitting parameters, with their associated errors, were obtained and then used to calculate the grain-boundary diffusion coefficient.

Figure 20 shows the logarithm of normalized, average chromium concentration versus $x^{6/5}$ at 1250^{0}C for both undoped and doped alumina, where x is the depth. Note that the assumed power-law behavior accurately describes the profile at large penetration depths.

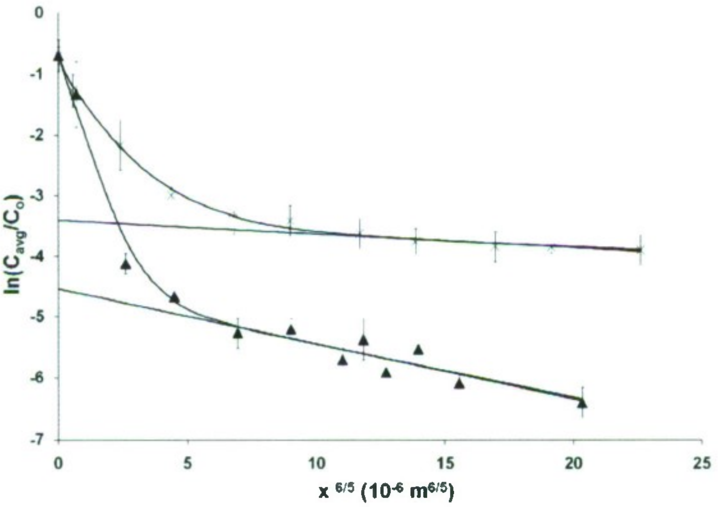

Figure 20: The logarithm of the normalized average concentration versus $x^{6/5}$ for both undoped and Y-doped alumina at 1250 ^oC, where x is the diffusion depth.

To obtain activation energies and corresponding prefactors in an Arrhenius description of grain-boundary diffusion, the extracted diffusion coefficients were plotted versus reciprocal temperature in Figure 21.

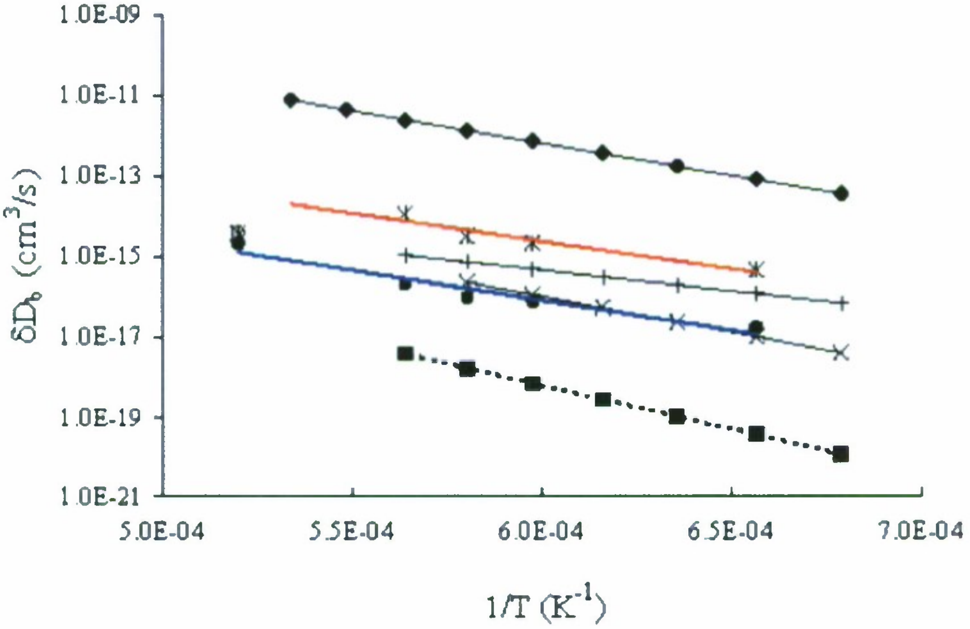

Figure 21: Arrhenius plot for δD_b parameters in alumina. i) δD_b (Al) in alumina (indirect determination)[1] (■), *ii) δD_b (Cr) in 100ppm Y-doped alumina (this work)* (●), *iii) δD_b(Cr) in undoped alumina (this work)* (*), *iv) δD_b(Cr) at 1650 °C in undoped alumina (this work)* (☼), *v) δD_b (Cr) in undoped alumina*[2] (x), *vi) δD_b (Cr) in 0.1 mol% Y-doped alumina*[2] *(+), vii) δD_b (Cr) in undoped alumina bicrystal*[3] (♦). *(1. Cannon et al., J. Amer. Ceram. Soc.,63, 46-53 (1980), 2. Lagrange et al., Ann. Chim. Fr., 12, 9-21(1987), 3. Stubican and Osenbach, Adv. in Ceramics, 10, 406-17 (1984).)*

For comparison, also shown are selected diffusivity data taken from the literature. Our data obey the expected Arrhenius relationships, except perhaps for the point at 1650^{0}C for undoped alumina. Upon close examination of the microstructure and associated electron backscattered diffraction in this case, it appears, from the wavy nature of the grain boundaries and from the spatial distribution of chromium near the boundaries, that diffusion-induced grain-boundary migration is occurring here. The weighted linear regression fit of our data to the Arrhenius equation yields a grain-boundary diffusivity D_b for a boundary of width δ for the undoped and doped cases, respectively (in cm^3/s):

$$\delta D_b = (4.77 \pm 0.24) \times 10^{-7} \exp\left(-\frac{264.78 \pm 47.68 \text{ (kJ/mol)}}{\text{RT}}\right)$$

$$\delta D_b = (6.87 \pm 0.18) \times 10^{-8} \exp\left(-\frac{284.91 \pm 42.57 \text{ (kJ/mol)}}{\text{RT}}\right)$$

The results indicate that chromium diffuses more rapidly in the undoped alumina samples, due primarily to a larger associated diffusion prefactor. It should also be noted that the ratio of the grain-boundary diffusivity to the bulk diffusivity is > 10^4 for both aluminum self-diffusion and for chromium diffusion in alumina (where $\delta = 5$ nm is used). Having extracted activation energies for cation diffusion in alumina, it is also of interest to relate the results obtained here to creep studies where grain-boundary diffusion may be important. From several investigations it is clear that most of the activation energies obtained for creep are larger than those obtained from our results, as well as other direct diffusion studies. Given that the activation energies for creep (about 483 kJ/mole for undoped alumina) differ in magnitude from those found here, and change upon doping, we may infer that while the inhibition of grain-boundary diffusion due to doping may be partly responsible for creep retardation in these systems, other activated processes are also likely important.

E. Modeling and Simulation

The modeling and simulation component of this work involves developing analytical models and numerical procedures to model the effect of microstructural parameters, as well as reactive elements, on grain-boundary diffusion in alumina.

Using the finite difference (FD) method, a lattice grid is superimposed on the diffusion domain, and conservation equations written for fluxes in and out of each lattice point. The grain boundaries, represented by a uniform region only a few lattice points wide, are similarly treated by enforcing flux-balance boundary conditions along the interface. The system of equations are then assembled into a matrix and solved iteratively to obtain the spatial and temporal evolution of the diffusant. The method was first verified for an ideal model consisting of a single isolated grain boundary embedded between two columnar grains. Approximate analytical solutions have been obtained for this system for various boundary conditions assuming a simplified concentration profile in the grain boundaries (such as no preferential segregation of diffusant in the boundaries). The diffusion profile for the numerical model, consisting of a fixed concentration of diffusant applied to one end of the bicrystal, and a zero-flux boundary condition enforced at the other free surface, compared very well with the approximate analytical solutions in literature.

A more realistic model of diffusion in polycrystals reflects the complexity of the underlying microstructure. To represent this, a Voronoi network is created from *N* randomly distributed seeds, each corresponding to a different grain. These seeds are then grown at a constant radial growth rate, in this case on a square lattice, until impingement occurs with a neighboring grain. Each lattice site is associated with a particular grain or grain boundary. It was assumed that the microstructure was initially diffusant-free, and that the edges of the simulation cell were in contact with a constant source. The diffusive behavior of the generated microstructure is quantified by obtaining uptake curves as a function of time for different ratios of grain boundary to lattice diffusivities. The uptake curves were obtained by summing the diffusant concentration at all lattice points, except for grain boundary and source sites, and then normalizing by the total system area. Averages of microstructural uptakes are computed from an ensemble of microstructures, with each realization generated from a different random distribution of the *N* seeds.

Approximate analytical solutions to the numerical model described above were obtained by representing the system as a collection of circular grains with grain-area distribution identical to that obtained from a population of over 66000 grains in the Voronoi network. This distribution follows a one-parameter gamma function having a variance σ^2 =0.446. The analytical uptakes are obtained by averaging over the distribution of grain radii. For the case when the grain boundary diffusivity is much larger than bulk diffusivity, the grains act as independent grains, each subject to some constant source around the perimeter. Otherwise, it is important to specify a function representing the time-dependent grain boundary filling function. Figures 22a and 22b below shows a comparison of the numerical and analytical solutions for the system described above for $\Delta_r=10^3$ and $\Delta_r \geq 10^4$, where Δ_r is the ratio of the grain boundary to lattice diffusivities. Each curve represents an average over 250 realizations of the microstructure. Note the good agreement over the wide range of times. Bars indicate the range of individual uptake curves, obtained from the 250 runs used in computing the average.

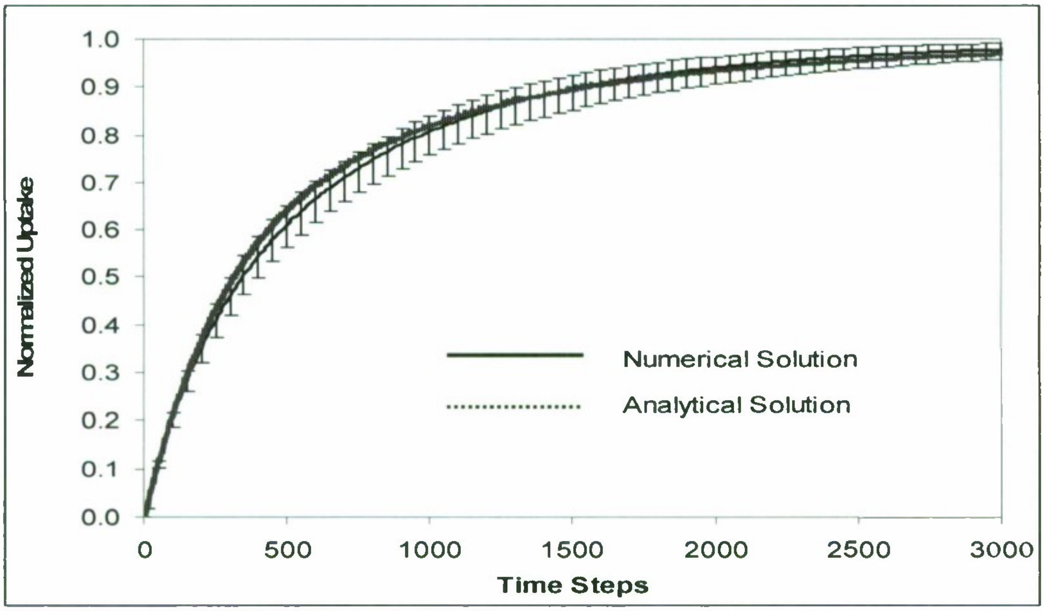

Figure 22a. A comparison of numerical and analytical uptake curves for $\Delta_r=10^3$.

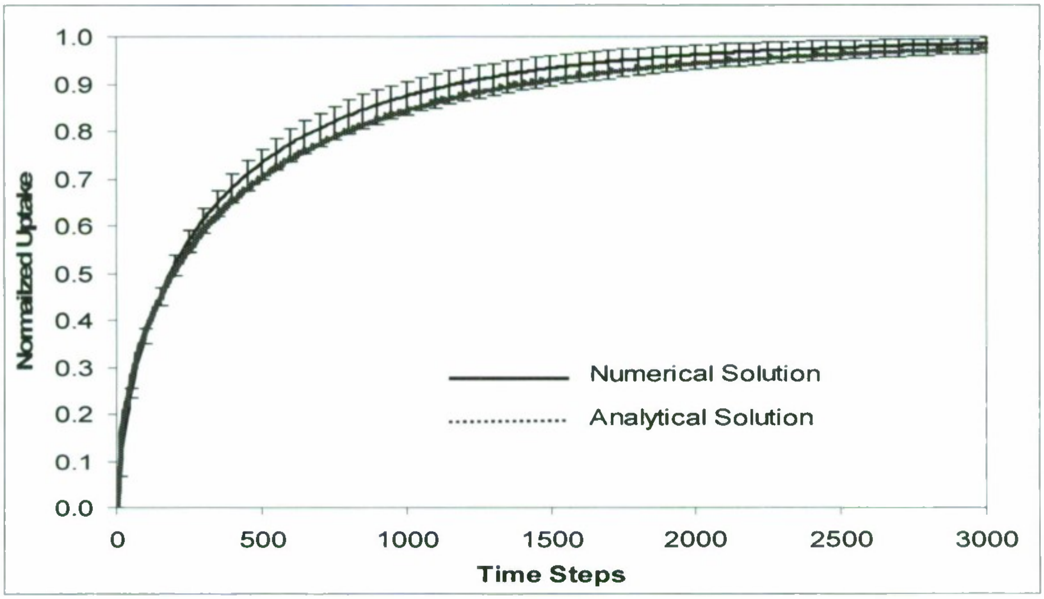

Figure 22b. A comparison of numerical and analytical uptake curves for $\Delta_r = 10^4$.

Molecular Dynamics Simulation of Inhibited Grain-Boundary Diffusion

Currently, it is of interest to incorporate other microstructural properties such as grain growth and diffusion with depletion/generation of species. Furthermore, we are interested in including the effects of boundary structure and anisotropy in microstructure. This will make it possible to study explicitly phenomena such as segregation of diffusant or impurities in the grain boundary, and the effect on grain-boundary diffusion.

From our earlier studies of Cr^{3+} [5] and oxygen [1,2] diffusion in doped alumina, it was suggested that segregating dopants may inhibit diffusion by blocking nominally fast paths along boundaries. Indeed, recent Monte Carlo simulations by Kansuwan and Rickman [6] confirm that the blocking of diffusion pathways can significantly alter the diffusion coefficient for relatively simple models of grain-boundary geometry. Nevertheless, for more realistic boundary models, the mechanisms for hindered diffusion remain unclear, and so we are undertaking large-scale molecular dynamics simulations of grain-boundary transport in doped alumina.

For this purpose, we have employed an empirical, interatomic potential to describe the interactions among aluminum, dopant and oxygen atoms. Given the relatively high activation energies for diffusion in these systems, we are using temperatures of around 2000K in our simulations. In our preliminary investigations, we are considering, for simplicity, the diffusion of aluminum and oxygen ions along a special boundary, namely the $\Sigma 13$ boundary on the basal plane of alumina. It is anticipated that the later incorporation of dopant ions will occur preferentially at the larger voids near the boundary in this structure.

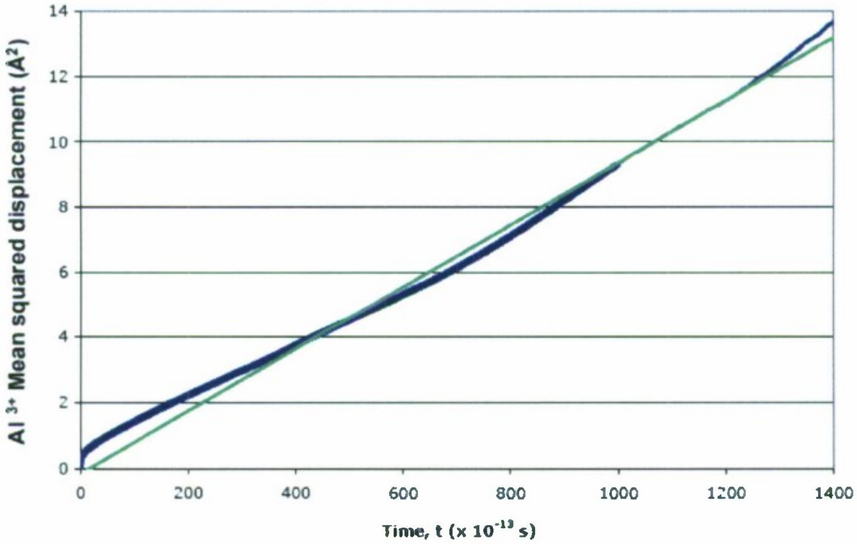

Figure 23: The mean-squared displacement of aluminum ions in the $\Sigma 13$ grain-boundary region as a function of time (blue curve). Also shown is the best linear fit to the data (green curve).

The diffusion coefficients for aluminum and oxygen ions can be calculated from the mean-squared displacements, $\langle r^2(t) \rangle$, of mobile ions versus time, t, in the vicinity of the grain boundary. Figure 23 shows the mean-squared displacement of aluminum ions versus time for ions near a $\Sigma 13$ boundary. The slope of this curve at late times yields the desired diffusion coefficient. Our aim to is to repeat these calculations for doped alumina using different concentrations of trivalent dopants (e.g., yttrium), and to quantify the aforementioned blocking effect from the trajectories of the diffusion ions.

References

1. H. Cheng, S. Dillon, H. Caram, J.M, Rickman, H.M. Chan and M.P. Harmer, " The Effect of Yttrium on Oxygen Grain-Boundary Transport in Polycrystalline Alumina Measured Using Ni Marker Particles," J.Amer. Ceram. Soc., **91** 2002-2008 (2008)

2. H. Cheng , H. S. Caram, W. E. Schiesser, J. M. Rickman, H. M. Chan and M. P. Harmer. "Oxygen Grain-Boundary Transport in Polycrystalline Alumina Using Wedge-geometry Bilayer Samples: Effect of Y-Doping," Acta Mater., [58], 2442-2451 (2010)

3. W.W. Mullins, "Theory of Thermal Grooving," J. Appl. Phys. 28, 333-39 (1957)

4. K. Bedu-Amissah, J.M. Rickman, H.M. Chan, and M.P. Harmer, "Impact of microstructure on grain boundary diffusion in polycrystals," J. Appl. Phys., 063511 (2005).

5. K. Bedu-Amissah, J.M. Rickman, H.M. Chan, and M.P. Harmer, "Grain-Boundary Diffusion of Cr in Pure and Y-doped Alumina," J. Am. Ceram. Soc. 90, 1551-1555 (2007).

6. P. Kansuwan and J. M. Rickman, "The Role of Segregating Impurities in Grain-Boundary Diffusion," J. Chem. Phys. 126, 094707 (2007).

7. S.J. Dillon, M. Tang, W.C. Carter and M.P. Harmer, "Complexion: A New Concept for Kinetics Engineering in Materials Science and Beyond," Acta Mater., [55], 6208-6218 (2007)

8. S.J. Dillon and M.P. Harmer, "Multiple Grain Boundary Transitions in Ceramics: A Case Study of Alumina," Acta Mater., [55], 5247-5254 (2007)